remote sensing

MDPI

Article

The Geological Investigation of the Lunar Reiner Gamma Magnetic Anomaly Region

Junhao Hu [1], Jingwen Liu [2], Jianzhong Liu [2,*], Jiayin Deng [3,4], Sheng Zhang [2], Danhong Lei [2], Xuejin Zeng [2] and Weidong Huang [2]

[1] School of Architectural Science and Engineering, Guiyang University, Guiyang 550005, China; hujunhaogyu2023@gmail.com
[2] Center for Lunar and Planetary Sciences, Institute of Geochemistry, Chinese Academy of Sciences, Guiyang 550081, China; liujingwen@mail.gyig.ac.cn (J.L.); zhangsheng@mail.gyig.ac.cn (S.Z.); leidanhong@mail.gyig.ac.cn (D.L.); zengxuejin@mail.gyig.ac.cn (X.Z.); huangweidong@mail.gyig.ac.cn (W.H.)
[3] School of Civil Engineering and Architecture, Henan University of Science and Technology, Luoyang 471000, China; 20b@igsnrr.ac.cn
[4] State Key Laboratory of Resources and Environmental Information System, Institute of Geographic Sciences and Natural Resources Research, Chinese Academy of Sciences, Beijing 100101, China
* Correspondence: liujianzhong@mail.gyig.ac.cn; Tel.: +86-18786617851

Abstract: Reiner Gamma is a potential target for low-orbiting spacecraft or even surface-landed missions in the near future. Unfortunately, thus far, no comprehensive low-altitude (below 20 km) or surface measurements of the magnetic field, magnetic source and plasma environment have been made post-Apollo to complement and complete our understanding of the solar wind interaction with lunar magnetic anomalies and swirl formation. Acquiring the detailed geological knowledge of the Reiner Gamma region is significant for the above scientific targets. In this study, the following research work in the lunar Reiner Gamma magnetic anomaly region was carried out for the regional geological investigation: (1) topographic and geomorphologic analysis; (2) element, mineral, and sequence analysis; and (3) a 1:10,000 regional geological map analysis. Our work helps define measurement requirements for possible future low-orbiting or surface-landed missions to the Reiner Gamma area or similarly magnetized regions of the lunar surface.

Keywords: Reiner Gamma; lunar magnetic anomalies; 1:10,000 regional geological map; geomorphological feature

check for updates

Citation: Hu, J.; Liu, J.; Liu, J.; Deng, J.; Zhang, S.; Lei, D.; Zeng, X.; Huang, W. The Geological Investigation of the Lunar Reiner Gamma Magnetic Anomaly Region. *Remote Sens.* **2024**, *16*, 4153. https://doi.org/10.3390/rs16224153

Academic Editor: Giancarlo Bellucci

Received: 20 September 2024
Revised: 30 October 2024
Accepted: 3 November 2024
Published: 7 November 2024

Copyright: © 2024 by the authors. Licensee MDPI, Basel, Switzerland. This article is an open access article distributed under the terms and conditions of the Creative Commons Attribution (CC BY) license (https://creativecommons.org/licenses/by/4.0/).

1. Introduction

Although the Moon does not currently have a global magnetic field, the research on remanent magnetization in lunar rocks and crust demonstrated a substantial lunar surface field billions of years ago [1–7]. It may be helpful to understand key scientific issues, including the lunar heat loss [1,8], the basic dynamo theory of the lunar core and mantle [4,6], the presence of volatiles on the surface on the poles [9–11], and possibly paleo-solar wind studies [9,12], based on the understanding of the origin, intensity, and life-time of this global field. The magnetic anomaly fields have been detected over numerous portions of its crust, and most of these regions are located antipodal to large basins [2,13–21]. The dominant genesis hypotheses of these magnetic anomaly fields include ejecta deposits [21–26], thermoremanent magnetization from magmatic processes [2,9,27–30], and shock-remanent magnetization by large impacts [24,31]. Obtaining information about the magnetic source bodies of these anomalies involving the geometry, depth, formation time, and magnetic mineralogy can better constrain the timing and the strength of the lunar past dynamo field [5,9,21,29,32,33].

The lunar swirls, characterized by the sinuous pattern of albedo in the soil, play a valuable tool in investigating the Moon's lithospheric magnetic anomalies due to its unique

geologic features with magnetic and photometric anomalies [5,9,15,29,34,35]. Several mechanisms have been proposed for swirl formation including cometary impact effects [36], solar wind deflection model [37,38], electrostatic dust levitation and transport [39–41], and the magnetic sorting [42]. The above hypotheses usually involved a "mini-magnetosphere" that shields the surface from the darkening effects of the solar wind [35,37,43–46]. Moreover, the lunar swirls can be used to more carefully investigate the geometry, depth, and formation time of the source bodies, attributed to the shallow burial scale of the magnetic anomaly source body [5,28,29].

Reiner Gamma, located on the lunar nearside along the western edge of Oceanus Procellarum (center: 7.4°N, 301°E) (Figure 1), is perhaps the most well-known magnetic anomaly with 22 nT at 30 km altitude [20,47–50], but no theory for its formation has been accepted [14,26,28,29,32,51,52]. Moreover, the spatial resolutions of the GRAIL gravity map and modeling are insufficient to resolve the narrow (<1–5 km width) dike features that might be responsible for swirls [2] and the low-altitude with high-resolution lunar magnetic field measurements and surface field sampling at Reiner Gamma region are still unknown [9,15,47,53], which lead to the genesis debated of this magnetic anomaly. Therefore, the comprehensive geological investigation of this typical lunar swirl region is necessary for future surface-landed missions and low-altitude measurements, which would also provide an opportunity to determine with much higher accuracy the strength and direction of the dynamo field when Reiner Gamma formed [2,9].

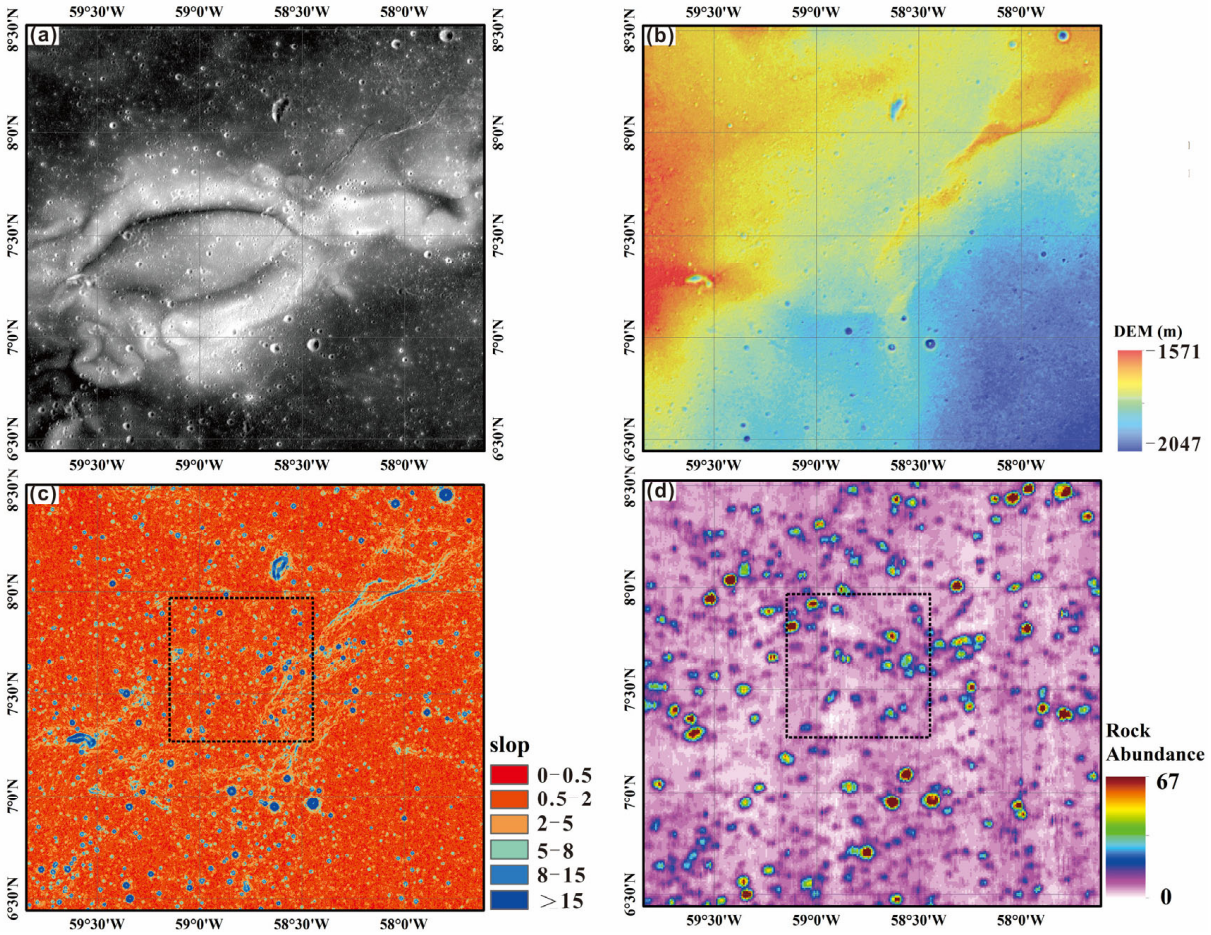

Figure 1. The background maps in Reiner Gamma region. (**a**–**d**) represent TOC, DEM, Slop, and Rock abundance in Reiner Gamma region, respectively.

From an engineering perspective, landing areas must ensure safe and reliable operations; at the same time, it is of great scientific significance [54]. Therefore, based on considerations of engineering safety, this article opted for a region characterized by a gentler slope (Figure 1c) and lower rock abundance (Figure 1d). Simultaneously, the scientific value of the area was also taken into account. Consequently, the 20 km by 20 km region located at the center of the Reiner Gamma area was chosen as the most suitable landing site (dash lines in Figure 1c,d), encompassing both bright and dark magnetic anomalies. This study analyzed the element compositions of the entire Reiner Gamma magnetic anomaly region to investigate its possible formation mechanisms and mineral contents. Detailed interpretations of the area's geological and topographical features were carried out to assess the feasibility of a safe landing and its geological background.

2. Data and Methods

2.1. Geochemical Composition Data

The Kaguya Multiband Imager acquired data in 9 ultraviolet–visible (UVVIS) to near-infrared (NIR) spectral bands (415, 750, 900, 950, 1001, 1000, 1050, 1250, 1550 nm), and covered a range of 65°N~65°S on the lunar surface. The instrument provided a spatial resolution of ~20 m per pixel for the first five spectral bands (UVVIS, 415–1001 nm), and ~62 m per pixel for the last four (NIR, 1000–1550 nm) at the nominal altitude of 100 km [55]. In this study, the abundances of the minerals (e.g., olivine, low/high-calcium pyroxene, and plagioclase) and the submicroscopic iron (SMFe) in Reiner Gamma magnetic anomaly region were from Lemelin et al. [55,56] and Taylor et al. [57], which were based on the MI data, respectively. Moreover, Lemelin et al. [55] downsampled the UVVIS data to the same spatial resolution as the NIR (~62 m per pixel) so that they could work with 9 spectral bands with matching spatial resolution. They also corrected systematic differences in the reflectance spectra between the first five spectral bands (UVVIS data) and the last four (NIR data) due to the differences in data source, and this data reduction method is explained in detail in Lemelin et al. [56].

Meanwhile, the abundances of the five major oxides (e.g., MgO, FeO, Al_2O_3, CaO, and TiO_2) in this study were taken from Zhang et al. [58]. To obtain good the correlation between MI spectral reflectance values and oxide content, the 1D-CNN algorithm was used by Zhang et al. [58]. Different from the MI data used in Lemelin et al. [55] and Taylor et al. [57], Zhang et al. [58] used eight bands (415 nm, 750 nm, 900 nm, 950 nm, 1001 nm, 1050 nm, 1250 nm, and 1550 nm) of the MI global mosaic for the calculation of the abundances of the five major oxides.

2.2. Topographic and Geomorphological Analysis Method

At present, the direct method for obtaining planetary topography is using a laser altimeter to send laser pulses from orbit and time the returning pulses [59–61]. In this study, the elevation data were obtained from the Chang'E-2 DEM, Lunar Orbiter Laser Altimeter (LOLA) [61,62] and the high-resolution SLDEM2015 [63]. The LOLA supplied highly accurate global coverage with a vertical precision of ~10 cm and an accuracy of ~1 m [61,62]. Furthermore, the resolution of LOLA is approximately 118 m per pixel. The SLDEM was combined by the LOLA and the SELENE TC data through the Kaguya teams and covers latitudes within ±60° with a horizontal resolution of ~59 m per pixel and a vertical accuracy of ~3 to 4 m [63]. In addition, the high-resolution image data collected through Chang'E-2 (7 m/pixel) and narrow-angle camera images (LROC NAC, M190987807RC, M190987807LC, M188628884RC, M186269979RC, M148550332RC, M1366273619RC, M1328688537RC, M1328688537LC, M1182857098LC, M1180506270RC, M1175794573RC, M1165201476LC, M1108661104RC, and M104898806RC, with a resolution of approximately 0.5 m/pixel) are used in this study. Considering the data resolution and the data size of subsequent data processing, this study used the DEM generated by LOLA to study the classification criteria of lunar relief amplitude in the target area of the Reiner Gamma region. The higher-resolution SLDEM data were used to verify the optimum

ranges of the lunar relief amplitude calculated from the LOLA DEM. And the data were downloaded from https://astrogeology.usgs.gov/search/map/moon_lro_lola_dem_118m, accessed on 11 March 2014 and https://astrogeology.usgs.gov/search/map/moon_lro_lola_selene_kaguya_tc_dem_merge_60n60s_59m, accessed on 4 February 2020.

The lunar surface is divided into five geomorphic types including very low altitude, low altitude, medium altitude, high altitude, and very high altitude [64]. Thresholds of −2500 m, −1500 m, 1000 m, and 3000 m, as proposed by Liu et al. (2021) [64], were used as elevation criteria in this study's lunar morphological classification system. Based on the LOLA data, this study calculates slope data for the Reiner Gamma region through the maximum average method [65]. Referring to general classification standards for Earth's topographic slopes and lunar surface landing cushioning safety requirements, areas on the lunar surface are categorized as follows: areas with an incline of less than 0.5° are considered plains, 0.5–2° as gentle slopes, 2–5° as gradual slopes, 5–8° as moderate slopes, and >8° as a hazardous area for lunar surface landing [66]. This study quantitatively analyzes the roughness of the Reiner Gamma region using the root mean square height difference method through the elevation data from Chang'E-2. And we calculated the RMS height at the window size of three pixels with the baseline of 60 m, through the 20 m/pixel resolution Chang'E-2 DEM [67].

To calculate the relief amplitude in this region, we determine the best window for relief amplitude calculation through the mean change-point method based on the Chang'E-2 20 m DEM data [68]. In general, the corresponding landforms in lunar surface are classified into seven types (e.g., minor microrelief plains, minor microrelief platforms, microrelief landforms, small relief landforms, medium relief landforms, large relief landforms, and extremely large relief landforms) according to relief amplitudes of 100 m, 200 m, 300 m, 700 m, 1500 m, and 2500 m [68]. The rock abundance in this study is inferred from diviner data obtained by LRO during its circular orbit phase from 3 October 2009 to 7 October 2011. Each pixel represents the fractional area fragments occupy within that lunar surface area. The algorithm considers the influence of local slopes on rock abundance inversion based on DEM terrain data acquired by LOLA [69]. Ultimately, this study delineates suitable areas for lunar surface-landed activities based on a comprehensive acquisition of terrain and landform characteristics within the Reiner Gamma region.

2.3. Mapping the 1:10,000 Geological Map

Chinese researchers have completed the compilation of the 1:2.5 Million Lunar Geological Map and achieved remarkable international recognition including the lunar geological maps, the lunar lithologic maps and the lunar tectonic maps [70–74]. Based on the 1:2.5 Million Lunar Geological Map, we have mapped out the geologic structures, rocks and crater units in the target of the Reiner Gamma region with 1:10,000-scale through the high-resolution geochemical composition data, image data, and the DEM data collected and produced in 2.1 and 2.2. The main mapping processes are as follows:

(1) Scale determination: the decision to use a 1:10,000 scale for the Reiner Gamma region was carefully considered to balance the need for detailed geological information with the practical limitations of data resolution and map readability. And the primary consideration was the resolution of the image data utilized. This decision was carefully weighed to harmonize the demand for detailed geological information with the practical constraints of data resolution and map readability. The resolution of the image data is crucial due to its impact on the identification and depiction of key geological structures, such as the ejecta blankets' boundaries of impact craters, magnetic anomaly boundaries, impact crater chains, and lunar rilles. High-resolution data provide intuitive and granular insights into surface features, forming an essential foundation for geological research and analysis. Therefore, the selected scale of 1:10,000 ensures that the map captures the necessary details without compromising readability, thereby maximizing the scientific value and accuracy of the geological information conveyed.

(2) Determination of map content representation: this included not only all the geological structures in the 1:2.5 Million Lunar Geological Map but also the magnetic anomaly bands in this region.
(3) Development of standards and specifications for legends and symbols: the majority of the legends and symbols were inherited from the 1:2.5 Million Lunar Geological Map with the modifications made to represent lunar ridges and rilles as areal structures. Additionally, graphical legends for magnetic anomaly bands have been included.
(4) Establishment of base map databases: through the ArcGIS 10.8, we have created a gdb (geodatabase) file and subsequently established multiple feature classes based on the attribute tables and classifications of geological units from the 1:2.5 Million Lunar Geological Map. Each feature class corresponds to a specific geological unit, thereby organizing the data into distinct groups of feature types.
(5) Geological mapping: the identification and expression of lunar structures, igneous rocks, impact ejecta, and the age of various factors.
(6) Map compilation: establish a mapping template based on the ArcGIS, graphically edit the map units, and label with annotations.
(7) Quality control: topology checking and manual checking.
(8) Map finalization and output.

2.4. Stratigraphic Analysis of the Reiner Gamma Region

The large-scale topography in the article, such as the age of basalt and the age of basins, refers to the research results of China's 1:2.5 million geological map. As the diameter of small impact craters in the landing area is typically under 1 km, no database on their period currently exists. By analyzing radiation patterns, internal morphology, rock abundance, impact crater diameter, and relevant research (http://priede.bf.lu.lv/GIS/.Descriptions/RST/Sect19/nicktutor_19-5.shtml, accessed on 15 March 2024) and mapping experience, we established a relative age assessment criterion tailored for small, spatially isolated impact craters: (1) Craters with a diameter of less than 200 m are generally considered to be Copernican impact craters. (2) In craters with diameters of between 200 m and 500 m, those with extremely flat morphologies are classified as Eratosthenian, while the rest are Copernican. (3) Craters with diameters between 500 m and 1 km, featuring smooth crater walls and rocks distributed around their edges, are categorized as Copernican impact craters. In contrast, those relatively flat, situated close to each other, and lacking rocks are classified as Eratosthenian impact craters. (4) In craters with diameters between 1 km and 5 km, those displaying apparent ejecta radiation rays and a rich distribution of rocks at their edges are classified as Copernican impact craters. Craters with a small amount of rocks and well-preserved shapes are categorized as Erathonian impact craters, while those with flat shapes and certain damage are classified as Imbrian impact craters.

The depths of impact craters in the stratigraphic sequence have been exaggerated for clarity. Typically, the depth of smaller craters is approximately one-tenth of their diameter, but in this article, it has been exaggerated to one-fourth to one-third. The thickness of the basalt is based on research findings from other studies. The thickness of the ejecta in the two large basins at the bottom is determined using Housen's model [75].

3. Results

3.1. Geochemical Compositions in the Reiner Gamma Region

As shown in Figure 2a–e, the MgO content ranges from 5.1 to 13.5 wt%, FeO content ranges from 6 to 23 wt%, Al_2O_3 content ranges from 9.5 to 21.2 wt%, CaO content ranges from 9.3 to 13.2 wt%, and TiO_2 content ranges from 2.5 to 9.6 wt%. Compared to the dark lanes of the Reiner Gamma swirl and the surrounding mare regions, the bright lobes of the swirl have higher contents of MgO, CaO, and Al_2O_3 and significantly lower FeO, TiO_2, and submicroscopic iron (SMFe) contents (Figure 2). The contents of olivine, orthopyroxene, clinopyroxene, plagioclase, and SMFe are 0–48 wt%, 0–74 wt%, 0–60.8 wt%, 14–63 wt%, and 0.5–7 wt%, respectively (Figures 2f and 3a–d). The bright labels of the swirl have lower

contents of olivine, orthopyroxene, and clinopyroxene and higher contents of plagioclase compared to the dark lanes of the Reiner Gamma swirl and the surrounding mare regions (Figure 3a–d).

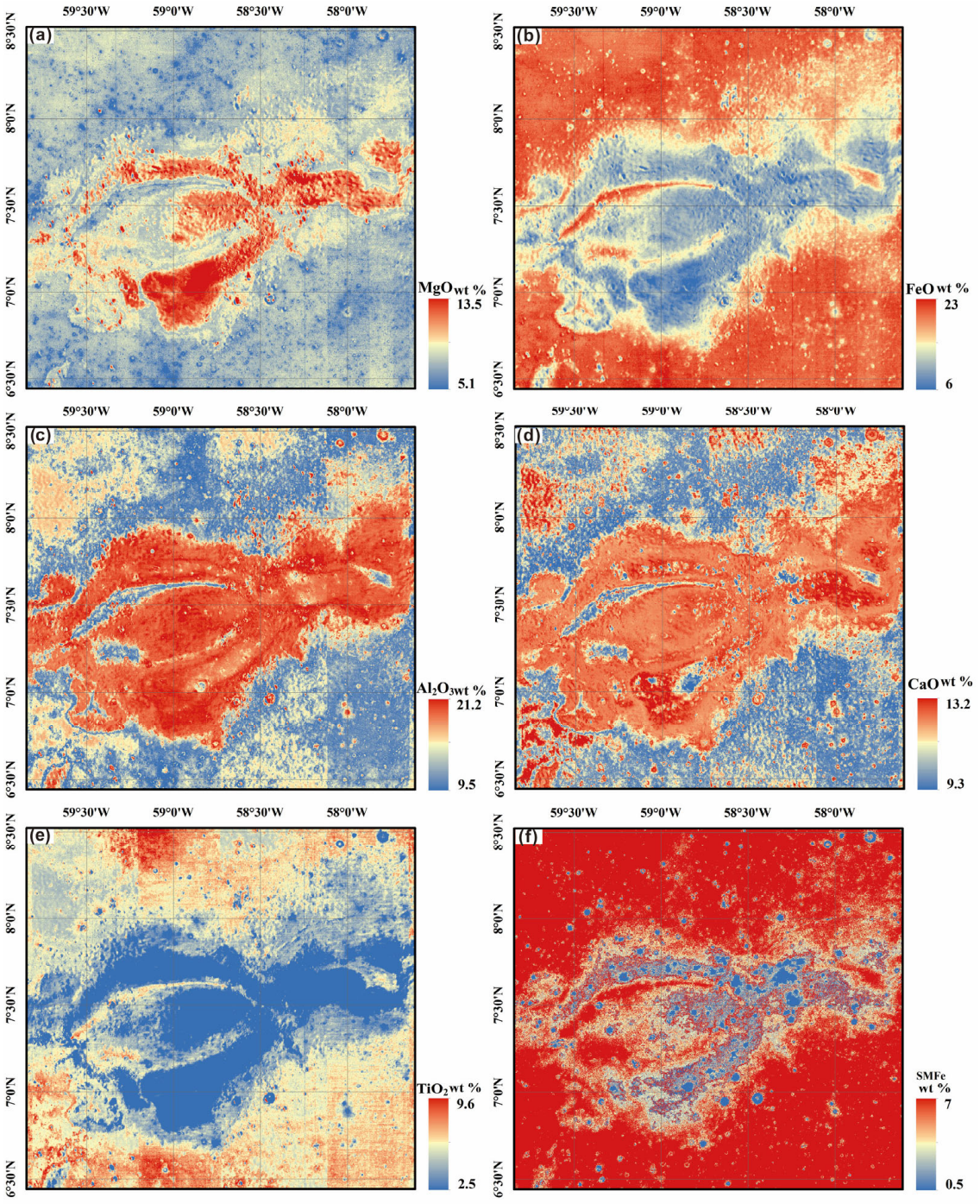

Figure 2. The major element compositions in the Reiner Gamma region. (**a**–**f**) represent the MgO, FeO, Al_2O_3, CaO, TiO_2, and SMFe contents in Reiner Gamma region, respectively.

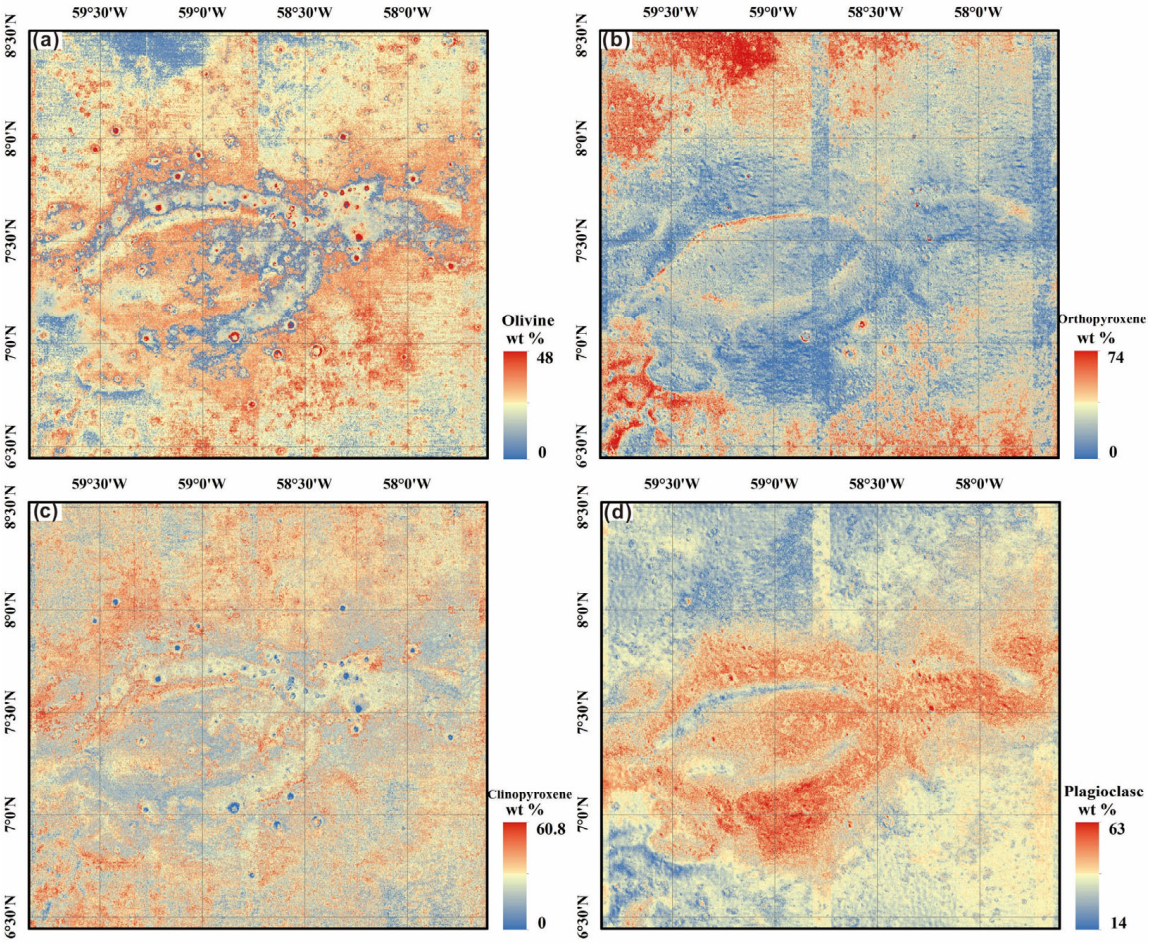

Figure 3. The major mineral compositions in the Reiner Gamma region. (**a**–**d**) represent the olivine, orthopyroxene, clinopyroxene, and plagioclase contents in Reiner Gamma region, respectively.

3.2. Topographic and Geomorphological Parameters of the Target in Reiner Gamma Region

The Reiner Gamma magnetic anomaly area belongs to a low-altitude region with the elevation ranging from −2041 m to −1548 m (Figure 1b). The eastern region of this lunar swirl is suitable for surface-landed missions due to its high quality in geological characters (Figure 4a). It ranges from −1833.96 m to −1685.96 m in altitude (Figure 4b). As can be seen from the slope map (Figure 4c), it is evident that the slopes in this region vary moderately with most parts ranging from 0 to 5 degrees in larger areas and smaller areas ranging from 5 to 15 degrees. The overall roughness values range between 0 and 1.5 m with some local areas exceeding 1.5 m (Figure 4d). Additionally, there are 58 craters larger than 300 m in diameter, which indicates a relatively low crater density in this region (Figure 4a). The average rock abundance is 5.5 with a maximum value of 67%, which suggests low rock abundance (Figure 4e). Regarding basic landform types (Figure 4f), the blue areas represent minor microrelief plains with the highest safety level, which cover the majority of the map; the yellow areas represent microrelief landforms with some degree of hazard extant, which are sparsely distributed on the map; and the red areas represent small relief landforms that are the most dangerous regions, but these are extremely limited in distribution.

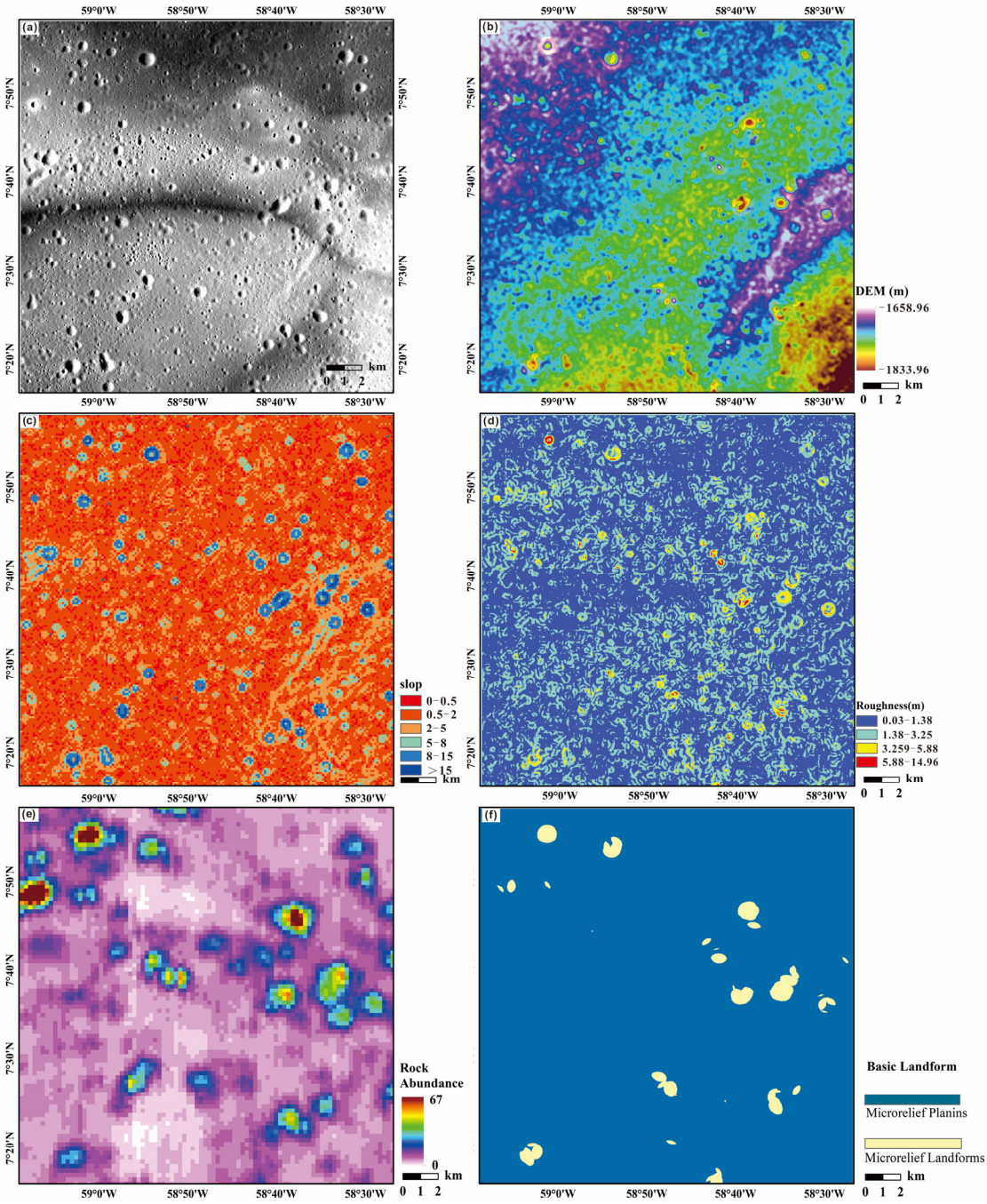

Figure 4. Topographic and geomorphological parameters in the target of the Reiner Gamma region. (**a**,**b**) represent NAC and DEM maps in the target of the Reiner Gamma region. (**c**–**f**) represent the slop, roughness, rock abundance, and basic landforms in the target of the Reiner Gamma region, respectively.

3.3. The 1:10,000 Geological Map of the Target in Reiner Gamma Region

By combining imaging data with a resolution better than 1 m, DEM with a spatial resolution better than 20 m and the compositional data, the 1:10,000 geological map of the target area in the Reiner Gamma magnetic anomaly region (20 km by 20 km) was created (Figure 5). This geological map includes 60,319 impact craters with diameters ranging from 10 to 100 m. There are 934 craters of the Copernican Period with diameters of over 100 m, 585 craters of the Eratosthenian Period with diameters of over 100 m, 12 craters of unknown age with diameters of over 100 m, and 55 craters of the Imbrian Period with diameters of

over 100 m. This map also contains one basalt unit, four linear ridge structures, six domes and twenty-four impact crater chains (Figure 5).

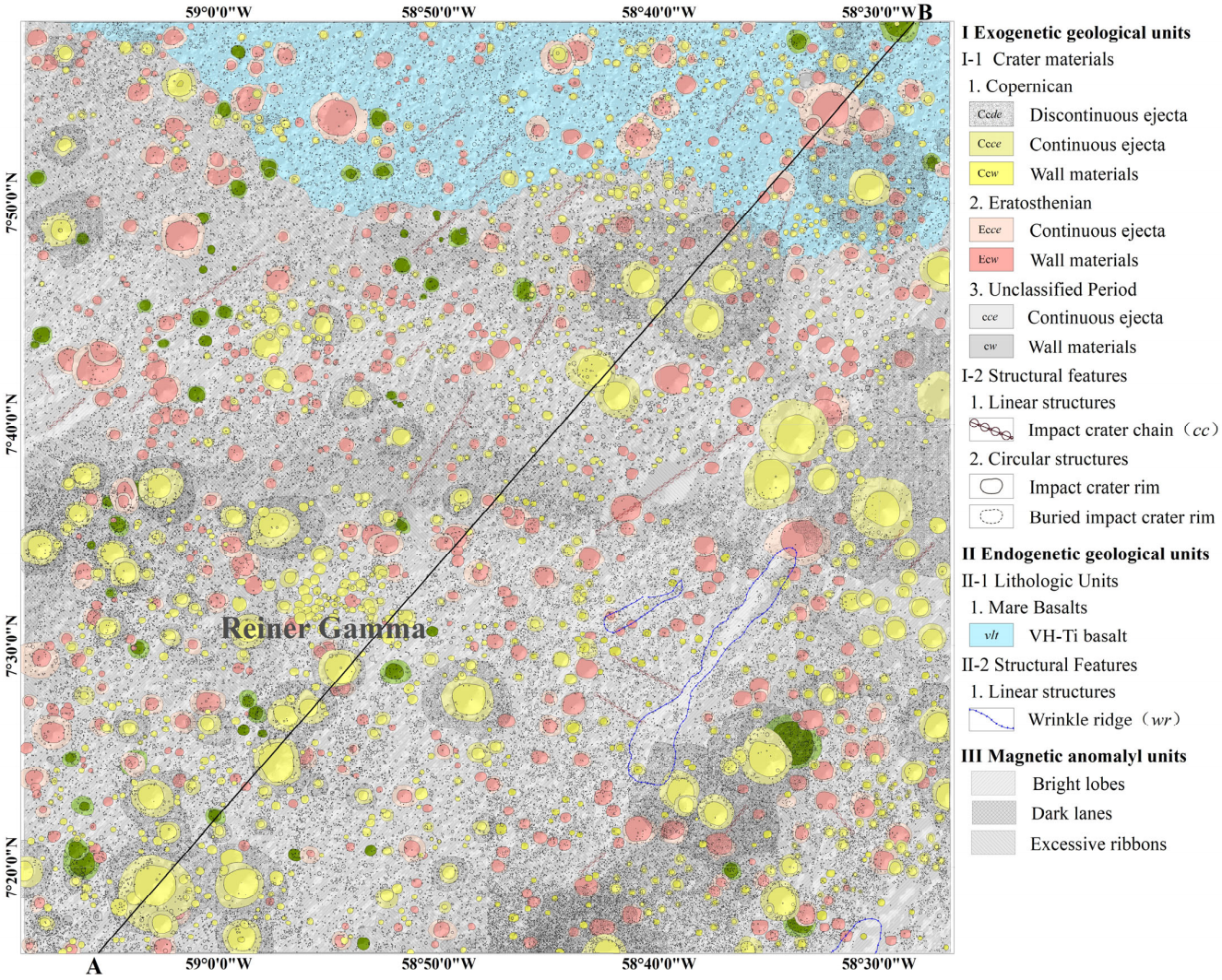

Figure 5. The 1:100,00 geologic map of the target in the Reiner Gamma region. The "AB" represents the section line which traverses the major geological tectonics and the main magnetic anomaly units of this region (600 dpi in https://zenodo.org/uploads/14003443, accessed on 28 October 2024).

3.4. The Stratigraphic Sequence Within the Target of the Reiner Gamma Region

As shown in Figure 6, the lowest layer in this area is composed of ferroan anorthosites formed in the Magma–Oceanian Period. During the Aitkenian Period, the Reiner Gamma region experienced continuous ejecta deposition from the Grimaldi basin to the southwest and the Flamsteed–Billy basin to its southeast, which overlayed the ferroan anorthosites. No material from the Nectarian or Imbrian Period was observed in the Reiner Gamma region. Following the formation of the Imbrium basin, extensive volcanic activities occurred in this region during ~3.9 Ga to 3.5 Ga [76,77]. Subsequently, a small-scale eruption of low-titanium basalts occurred in the Reiner Gamma region (3.30 Ga) [77]. During the later modification stage (3.16 Ga to the present), the basalts underwent modification from small-scale impact events and space weathering, which generated various types of impact craters in the region. Due to the differences in surface lithology and the alteration resulting from space weathering, significant differences in the thickness of surface regolith are observed in the basaltic and volcanic breccia areas [78].

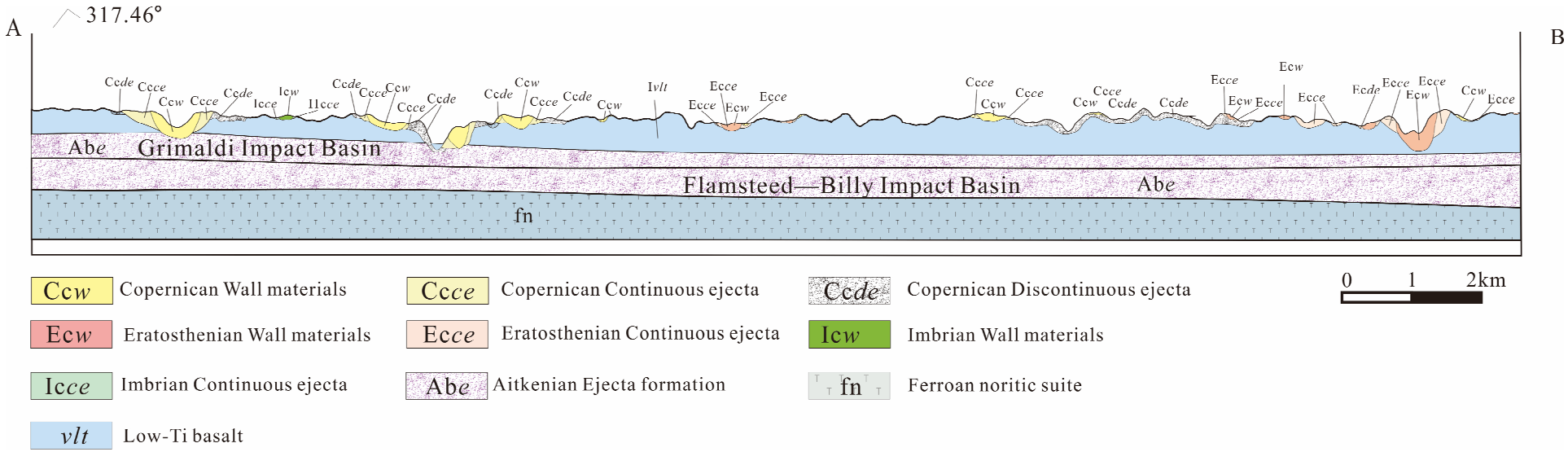

Figure 6. The stratigraphic sequence of the target in the Reiner Gamma region.

4. Discussion

4.1. Geochemical Features of the Reiner Gamma Region

Recent studies have proposed that the formation of the Reiner Gamma swirl may be related to the interaction between the mini-magnetosphere and the solar wind plasma [12,34,42,46,79,80], and the optical anomalies in this region are primarily attributed to differences in lunar soil maturity [34,81]. Figures 2 and 3 show no significant differences in the element contents and mineral compositions between the dark lanes of the Reiner Gamma swirl and the surrounding lunar mare, which is in accordance with similar spectral characteristics [81]. However, the bright lobes of Reiner Gamma have higher MgO, Al_2O_3, and CaO contents and lower FeO and TiO_2 contents compared to the dark lanes and the surrounding lunar mare (Figure 2a–e). Additionally, the bright lobes have lower olivine, orthopyroxene, and clinopyroxene contents, but higher plagioclase content compared to the above regions (Figure 3). These characteristics are also reflected in the spectral and photometric differences between the bright lobes, dark lanes, and the surrounding lunar mare [35,81]. Moreover, the bright lobes of the Reiner Gamma swirl have significantly lower SMFe content compared to the dark lanes and the surrounding lunar mare (Figure 2f). The features above may corroborate the idea that the reflectance differences in swirls are related to the interactions between the mini-magnetosphere and the solar wind plasma [46,80,82,83].

Existing research has shown the presence of ellipsoidal magnetic sources within the basalt in this area [2,5], and the types of magnetic minerals within these sources can reflect their origins [2,84–88]. However, the thickness of the overlying basalts with ~250 m to ~2.3 km [5] and the spatial resolution of the existing gravity data make it challenging to distinguish the origin of these magnetic sources [2], i.e., whether they are the melt sheet or floor deposits of an impact crater or slow cooling and sub-solidus reduction in lunar magmatic bodies. Therefore, surface-landing for the measurements of the field and plasma at Reiner Gamma is significant for understanding the magnetic mineralogy of the source bodies and further provides an opportunity for us to determine with much higher accuracy the strength and direction of the dynamo field when the Reiner Gamma formed [2,9,39].

4.2. Topographic and Geomorphological Features of the Target in the Reiner Gamma Region

The topographic and geomorphological features of the lunar surface are crucial for future surface-landed missions. The elevation and relief amplitude as the macroscopic morphological types reflect lunar terrain variations through composite matrices. The elevation variations of the target in the Reiner Gamma region range from −1833.96 m to −1685.96 m indicate that this area is low-altitude (Figure 4b). Simultaneously, in terms of basic landform types (Figure 4f), it is evident that the minor microrelief plains dominate most of the target region. Moreover, the slightly hazardous microrelief landforms areas occurrences sporadic, and the most hazardous regions of small relief landforms are only found in extremely isolated areas.

The slope and roughness are essential indicators for expressing terrain characteristics. The magnitude of the slope directly impacts the scale and intensity of surface material flow and energy conversion, which represents the local surface inclination. The target area in the Reiner Gamma region comprises gentle to gradual slopes, ranging broadly from 0 to 5°, with smaller sections composed of slopes between 5 and 15° (Figure 4c). Surface roughness serves as a crucial parameter in assessing the engineering feasibility of ground operations. It quantifies the degree of lunar surface erosion and spatial variations in lunar morphology and records geological activities such as erosion, subsidence, deposition, and infilling on planetary surfaces. As shown in Figure 4d, the roughness values in the target of the Reiner Gamma region range predominantly from 0 to 1.5 m with some local areas exceeding 1.5 m, which indicates that the selected target area comprises flat terrain. As can be seen from Figure 4e, rock abundance is relatively low except for a few areas with 5.5% on average and with a maximum value of 67%.

Moreover, there are only 58 impact craters larger than 300 m in diameter, which indicates a low crater density in this region. Meanwhile, four major wrinkle ridges oriented in a northeast direction are located on the bright streaks on the eastern side of the Reiner Gamma swirl. Other features including grooves, rilles, and gullies are relatively small in scale (Figure 5). In summary, the geological environments in the selected target are generally stable and mainly influenced by the infilling of mare basalts with relatively small-scale structural types and a few surrounding impact basins. Therefore, this target is highly favorable for surface-landing and in situ measurements of both magnetic fields and plasma within lunar crustal magnetic anomalies, which help us to understand the nature of anomalies and the various processes involved in space weathering.

4.3. Geological Evolution of the Reiner Gamma Region

4.3.1. Magma–Oceanian and Aitkenian Periods

The crystallization of the lunar magma ocean (LMO) led to the differentiation of the silicate portion into a dense ultramafic to mafic cumulate pile (the lunar mantle), and after ~70–80 percent solidification, the crystallization of plagioclase formed an anorthosite flotation crust that ultimately reached a thickness of up to ~60 km [39,89–94]; the crust in this region is presented in Figure 6. From a later stage (>90 PCS), a residual melt enriched with highly incompatible elements, including the heat-producing elements K, Th, and U, represents the source of the geochemical signature identified in various lunar lithologies (e.g., KREEP basalts) [93,95–98]. New laboratory and spacecraft measurements strongly indicate that the intensity of the magnetization is a result of an ancient core dynamo reached that of the present Earth between 4.25 to 3.56 billion years ago (Ga) [6,7,32]. The mechanisms for sustaining such an intense and long-lived dynamo are uncertain but may include mechanical stirring by the mantle and core crystallization [6]. During the Aitkenian Period (4.31–3.92 Ga), continuous ejecta from the Grimaldi basin to the southwest and the Flamsteed–Billy basin to the southeast of the Reiner Gamma region, were deposited onto the studied area, covering the primordial lunar crust composed of ferroan anorthosites.

4.3.2. Nectarian and Imbrian Periods (3.88~3.16 Ga)

No Nectarian Period rocks were exposed in the Reiner Gamma region. Furthermore, large-scale volcanic eruptions occurred in the area after the formation of the mare Imbrium basin (~3.9 Ga–3.5 Ga) [76,77,99,100]. Meanwhile, this period of volcanic activity coincides with the era of high magnetic fields on the Moon [6,9,32]. Subsequently, a small-scale low-titanium basaltic magma eruption occurred in the study region (~3.30 Ga) [77], and the field then declined by at least an order of magnitude by ~3.3 Ga [6,101–103]. Recent studies have suggested that the source of the magnetic anomaly in the Reiner Gamma region was located in the lower part of this low-titanium basalt, with the formation time between ~3.3 Ga and ~3.9 Ga, and the burial depth ranging from ~250 m to ~2.3 km [5,28,29]. The basal magnetic source might originate from thermoremanent magnetization generated by a subsolidus reduction associated with magmatic activity [2,5,28,50], or it could be related to a uniformly magnetized elliptical disk form from the melt sheet or floor deposits of an impact crater [9,21,26,51]. At the current stage, the spatial resolutions of the GRAIL gravity map and modeling are insufficient to resolve the narrow (<1–5 km width) dike features that might be responsible for swirls [2]. Therefore, surface landing could provide opportunities to constrain the magnetic source bodies' geometries and even the lunar dynamo's evolution.

4.3.3. Eratosthenian and Copernican Periods

After the mare basalt infilling process, the surface of the Reiner Gamma region was modified by small impact events and space weathering, which formed the various types of impact craters. Due to the differences in surface rock composition, distinct thicknesses of lunar regoliths formed in the basalt and volcanic breccia regions [78]. The Marius Hills located northwest (~150 km) of the Reiner Gamma swirl experienced continuous volcanic

activity during 1.03–3.65 Ga [104,105], with the volcanic activity in the region near the tail of the Reiner Gamma swirl occurring between 1.3–3.3 Ga [104]. Reiner Gamma's magnetic source bodies were also demagnetized by the heat from volcanic domes in the Marius Hills during this time [5,104], which may indicate that the dynamo that was only episodically strong [1] or that the dynamo existed in a weakened state [106].

5. Conclusions

The selected target for future surface-landing is located in the eastern Reiner Gamma magnetic anomaly region. This target is a low-altitude area, containing mostly minor microrelief plains. The geological environments in this area are generally stable and mainly influenced by the infilling of mare basalts with relatively small-scale structural types and few surrounding impact basins. Meanwhile, this target includes both the bright lobes and dark lanes of the Reiner Gamma. Therefore, considering the geological and geochemical features, the target could be a good location for a possible future low-orbiting or surface-landed mission in order to understand the nature of magnetic anomalies and the various processes involved in space weathering.

Author Contributions: Conceptualization, J.H., J.L. (Jingwen Liu), and J.L. (Jianzhong Liu); methodology, J.D.; software, J.L. (Jingwen Liu); validation, J.H. and J.L. (Jingwen Liu); formal analysis, J.L. (Jingwen Liu); investigation, J.L. (Jingwen Liu), D.L., S.Z., W.H., and X.Z.; resources, J.L. (Jingwen Liu); data curation, J.L. (Jingwen Liu); writing—original draft preparation, J.H. and J.L. (Jingwen Liu); writing—review and editing, J.H., J.L. (Jingwen Liu), and J.L. (Jianzhong Liu); visualization, J.L. (Jingwen Liu); supervision, J.L. (Jianzhong Liu); project administration, J.L. (Jianzhong Liu); funding acquisition, J.L. (Jianzhong Liu). All authors have read and agreed to the published version of the manuscript.

Funding: This work was funded by the Supported by the National Key Research and Development Program of China (grant no. 2022YFF0503100), Compilation of Chinese Regional Geological Chronicles and Series of Maps (grant no. DD20221645), the Guizhou Provincial Basic Research Program (Qian Ke He basic-ZK [2021] general type 206 and Qian Ke He basic-ZK [2024] general type 670), the Guizhou Provincial Department of Education Higher Education Young Science and Technology Talent Growth Program (Qian Jiao He KY [2020] 077), the Guizhou Province High-Level Innovative Talent-Thousand-Level Project (GCC [2023] 019), and the Guiyang University Talent Introduction Startup Fund Research Project-GYU-KY-[2024] (2019039510821).

Data Availability Statement: The LOLA DEM, LROC WAC, LROC NAC, SLDEM2015, and the abundance of olivine, low-calcium pyroxene, high-calcium pyroxene, plagioclase, and submicroscopic iron (SMFe) can be accessed through the Planetary Data System Geosciences Node (https://pds-geosciences.wustl.edu/dataserv/moon.html, accessed on 30 October 2024). The CE-2 data can be downloaded from the Chinese lunar and planetary data release system (https://moon.bao.ac.cn/ce5web/searchOrder-ce2En.do, accessed on 1 September 2019).

Acknowledgments: The authors are grateful to Jing-Wen Liu and Jian-Zhong Liu for their significant contributions to the conception and to the experimental support of this study. Many thanks to the Jia-Yin Deng for her data methods and to the engineers Sheng Zhang, Dan-Hong Lei, Xue-Jin Zeng, and Wei-Dong Huang for their data analyses.

Conflicts of Interest: The authors declare no conflicts of interest.

References

1. Evans, A.J.; Tikoo, S.M. An episodic high-intensity lunar core dynamo. *Nat. Astron.* **2022**, *6*, 325–330. [CrossRef]
2. Liang, Y.; Tikoo, S.M.; Krawczynski, M.J. Possibility of Lunar Crustal Magmatism Producing Strong Crustal Magnetism. *J. Geophys. Res. Planets* **2024**, *129*, e2023JE008179. [CrossRef]
3. Mighani, S.; Wang, H.P.; Shuster, D.L.; Borlina, C.S.; Nichols, C.I.O.; Weiss, B.P. The end of the lunar dynamo. *Sci. Adv.* **2020**, *6*, eaax0883. [CrossRef]
4. Scheinberg, A.L.; Soderlund, K.M.; Elkins-Tanton, L.T. A basal magma ocean dynamo to explain the early lunar magnetic field. *Earth Planet. Sci. Lett.* **2018**, *492*, 144–151. [CrossRef]
5. Seritan, M.R.K.; Garrick-Bethell, I. Volcanic thermal demagnetization of the Reiner Gamma magnetic anomaly. *Icarus* **2023**, *403*, 115601. [CrossRef]

6. Weiss, B.P.; Tikoo, S.M. The lunar dynamo. *Science* **2014**, *346*, 1246753. [CrossRef]
7. Zhai, K.; Yin, Y.; Zhai, S.M. Thermal and Dynamo Evolution of the Lunar Core Based on the Transport Properties of Fe-S-P Alloys. *Geophys. Res. Lett.* **2024**, *51*, e2024GL108131. [CrossRef]
8. Evans, A.J.; Tikoo, S.M.; Andrews-Hanna, J.C. The Case Against an Early Lunar Dynamo Powered by Core Convection. *Geophys. Res. Lett.* **2018**, *45*, 98–107. [CrossRef]
9. Garrick-Bethell, I.; Poppe, A.R.; Fatemi, S. The Lunar Paleo-Magnetosphere: Implications for the Accumulation of Polar Volatile Deposits. *Geophys. Res. Lett.* **2019**, *46*, 5778–5787. [CrossRef]
10. Green, J.; Draper, D.; Boardsen, S.; Done, C.F. When the Moon had a magnetosphere. *Sci. Adv.* **2020**, *6*, eabc0865. [CrossRef]
11. Tarduno, J.A.; Cottrell, R.D.; Lawrence, K.; Bono, R.K.; Huang, W.T.; Johnson, C.L.; Blackman, E.G.; Smirnov, A.V.; Nakajima, M.; Neal, C.R.; et al. Absence of a long-lived lunar paleo magnetosphere. *Sci. Adv.* **2021**, *7*, eabi7647. [CrossRef] [PubMed]
12. Poppe, A.R.; Garrick-Bethell, I.; Fatemi, S. Fractionation of Solar Wind Minor Ion Precipitation by the Lunar Paleomagnetophere. *Planet. Sci. J.* **2021**, *2*, 60. [CrossRef]
13. Baek, S.M.; Kim, K.H.; Garrick-Bethell, I.; Jin, H. Magnetic Anomalies Within the Crisium Basin: Magnetization Directions, Source Depths, and Ages. *J. Geophys. Res. Planets* **2019**, *124*, 223–242. [CrossRef]
14. Hood, L.L.; Torres, C.B.; Oliveira, J.S.; Wieczorek, M.A.; Stewart, S.T. A New Large-Scale Map of the Lunar Crustal Magnetic Field and Its Interpretation. *J. Geophys. Res. Planets* **2021**, *126*, e2020JE006667. [CrossRef]
15. Lee, J.-K.; Maxwell, R.; Jin, H.; Baek, S.-M.; Ghassemi, O.; Kelley, M.; Lee, H.; Kim, K.-H.; Lee, S.; Garrick-Bethell, I. A small lunar swirl and its implications for the formation of the Reiner Gamma magnetic anomaly. *Icarus* **2019**, *319*, 869–884. [CrossRef]
16. Maxwell, R.E.; Garrick-Bethell, I. Evidence for an Ancient Near-Equatorial Lunar Dipole From Higher Precision Inversions of Crustal Magnetization. *J. Geophys. Res. Planets* **2020**, *125*, e2020JE006567. [CrossRef]
17. Oliveira, J.S.; Wieczorek, M.A. Testing the axial dipole hypothesis for the Moon by modeling the direction of crustal magnetization. *J. Geophys. Res. Planets* **2017**, *122*, 383–399. [CrossRef]
18. Ravat, D.; Purucker, M.E.; Olsen, N. Lunar Magnetic Field Models From Lunar Prospector and SELENE/Kaguya Along-Track Magnetic Field Gradients. *J. Geophys. Res. Planets* **2020**, *125*, e2019JE006187. [CrossRef]
19. Shibuya, H.; Tsunakawa, H.; Takahashi, F.; Shimizu, H.; Matsushima, M.; Team, K.M.L. Near surface magnetic field mapping over the swirls in the SPA region using Kaguya LMAG data. In Proceedings of the European Planetary Science Congress, Rome, Italy, 19–24 September 2010; p. GP42A–03.
20. Tsunakawa, H.; Takahashi, F.; Shimizu, H.; Shibuya, H.; Matsushima, M. Surface vector mapping of magnetic anomalies over the Moon using Kaguya and Lunar Prospector observations. *J. Geophys. Res. Planets* **2015**, *120*, 1160–1185. [CrossRef]
21. Wakita, S.; Johnson, B.C.; Garrick-Bethell, I.; Kelley, M.R.; Maxwell, R.E.; Davison, T.M. Impactor material records the ancient lunar magnetic field in antipodal anomalies. *Nat. Commun.* **2021**, *12*, 6543. [CrossRef]
22. Crawford, D.A.; Schultz, P.H. Electromagnetic properties of impact-generated plasma, vapor and debris. *Int. J. Impact Eng.* **1999**, *23*, 169–180. [CrossRef]
23. Hood, L.L. Central magnetic anomalies of Nectarian-aged lunar impact basins: Probable evidence for an early core dynamo. *Icarus* **2011**, *211*, 1109–1128. [CrossRef]
24. Hood, L.L.; Artemieva, N.A. Antipodal effects of lunar basin-forming impacts: Initial 3D simulations and comparisons with observations. *Icarus* **2008**, *193*, 485–502. [CrossRef]
25. Tikoo, S.M.; Gattacceca, J.; Swanson-Hysell, N.L.; Weiss, B.P.; Suavet, C.; Cournède, C. Preservation and detectability of shock-induced magnetization. *J. Geophys. Res. Planets* **2015**, *120*, 1461–1475. [CrossRef]
26. Wieczorek, M.A.; Weiss, B.P.; Stewart, S.T. An Impactor Origin for Lunar Magnetic Anomalies. *Science* **2012**, *335*, 1212–1215. [CrossRef]
27. Garrick-Bethell, I.; Weiss, B.P.; Shuster, D.L.; Tikoo, S.M.; Tremblay, M.M. Further evidence for early lunar magnetism from troctolite 76535. *J. Geophys. Res. Planets* **2017**, *122*, 76–93. [CrossRef]
28. Hemingway, D.J.; Tikoo, S.M. Lunar Swirl Morphology Constrains the Geometry, Magnetization, and Origins of Lunar Magnetic Anomalies. *J. Geophys. Res. Planets* **2018**, *123*, 2223–2241. [CrossRef]
29. Kelley, M.R.; Garrick-Bethell, I. Gravity constraints on the age and formation of the Moon's Reiner Gamma magnetic anomaly. *Icarus* **2020**, *338*, 113465. [CrossRef]
30. Purucker, M.E.; Head, J.W.; Wilson, L. Magnetic signature of the lunar South Pole-Aitken basin: Character, origin, and age. *J. Geophys. Res. Planets* **2012**, *117*, 2011je003922. [CrossRef]
31. Bruck Syal, M.; Schultz, P.H. Cometary impact effects at the Moon: Implications for lunar swirl formation. *Icarus* **2015**, *257*, 194–206. [CrossRef]
32. Wieczorek, M.A.; Weiss, B.P.; Breuer, D.; Cébron, D.; Fuller, M.; Garrick-Bethell, I.; Gattacceca, J.; Halekas, J.S.; Hemingway, D.J.; Hood, L.L.; et al. Lunar Magnetism. *Rev. Mineral. Geochem.* **2023**, *89*, 207–241. [CrossRef]
33. Yang, X.; Wieczorek, M. Magnetic signatures of lunar impact craters. *Icarus* **2024**, *415*, 116049. [CrossRef]
34. Blewett, D.T.; Coman, E.I.; Hawke, B.R.; Gillis-Davis, J.J.; Purucker, M.E.; Hughes, C.G. Lunar swirls: Examining crustal magnetic anomalies and space weathering trends. *J. Geophys. Res.* **2011**, *116*, 2010je003656. [CrossRef]
35. Hemingway, D.; Garrick-Bethell, I. Magnetic field direction and lunar swirl morphology: Insights from Airy and Reiner Gamma. *J. Geophys. Res. Planets* **2012**, *117*, e2012je004165. [CrossRef]
36. Schultz, P.H.; Srnka, L.J. Cometary collisions on the Moon and Mercury. *Nature* **1980**, *284*, 22–26. [CrossRef]

37. Hood, L.L.; Schubert, G. Lunar Magnetic-Anomalies and Surface Optical-Properties. *Science* **1980**, *208*, 49–51. [CrossRef]
38. Hood, L.L.; Williams, C.R. The lunar swirls: Distribution and possible origins. In *Proceedings of the Lunar and Planetary Science Conference*; Cambridge University Press: Cambridge, UK, 1988; pp. 99–113.
39. Garrick-Bethell, I.; Lin, R.P.; Sanchez, H.; Jaroux, B.A.; Bester, M.; Brown, P.; Cosgrove, D.; Dougherty, M.K.; Halekas, J.S.; Hemingway, D. Lunar magnetic field measurements with a cubesat. In *Proceedings of SPIE Defense, Security, and Sensing*; SPIE: Bellingham, WA, USA, 2013.
40. Hendrix, A.R.; Greathouse, T.K.; Retherford, K.D.; Mandt, K.E.; Gladstone, G.R.; Kaufmann, D.E.; Hurley, D.M.; Feldman, P.D.; Pryor, W.R.; Stern, S.A.; et al. Lunar swirls: Far-UV characteristics. *Icarus* **2016**, *273*, 68–74. [CrossRef]
41. Rüsch, O.; Hess, M.; Wöhler, C.; Bickel, V.T.; Marshal, R.M.; Patzek, M.; Huybrighs, H.L.F. Discovery of a Dust Sorting Pro-cess on Boulders Near the Reiner Gamma Swirl on the Moon. *J. Geophys. Res. Planets* **2024**, *129*, e2023JE007910. [CrossRef]
42. Pieters, C.M.; Noble, S.K. Space weathering on airless bodies. *J. Geophys. Res. Planets* **2016**, *121*, 1865–1884. [CrossRef]
43. Bamford, R.A.; Kellett, B.; Bradford, W.J.; Norberg, C.; Thornton, A.; Gibson, K.J.; Crawford, I.A.; Silva, L.; Gargaté, L.; Bingham, R. Minimagnetospheres above the Lunar Surface and the Formation of Lunar Swirls. *Phys. Rev. Lett.* **2012**, *109*, 081101. [CrossRef]
44. Deca, J.; Divin, A.; Lue, C.; Ahmadi, T.; Horányi, M. Reiner Gamma albedo features reproduced by modeling solar wind standoff. *Commun. Phys.* **2018**, *1*, 12. [CrossRef]
45. Hood, L.; Coleman, P., Jr.; Wilhelms, D. The Moon: Sources of the crustal magnetic anomalies. *Science* **1979**, *204*, 53–57. [CrossRef] [PubMed]
46. Kurata, M.; Tsunakawa, H.; Saito, Y.; Shibuya, H.; Matsushima, M.; Shimizu, H. Mini-magnetosphere over the Reiner Gamma magnetic anomaly region on the Moon. *Geophys. Res. Lett.* **2005**, *32*, e2005gl024097. [CrossRef]
47. Blewett, D.T.; Halekas, J.; Ho, G.C.; Greenhagen, B.T.; Anderson, B.J.; Vines, S.K.; Regoli, L.; Jahn, J.M.; Kollmann, P.; Dene-vi, B.W. Lunar Vertex: PRISM Exploration of Reiner Gamma. In *Proceedings of 53rd Lunar and Planetary Science Conference*; Lunar and Planetary Institute: Houston, TX, USA, 2022; p. 1131.
48. Denevi, B.W.; Robinson, M.S.; Boyd, A.K.; Sato, H.; Hapke, B.W.; Hawke, B.R. Characterization of space weathering from Lunar Reconnaissance Orbiter Camera ultraviolet observations of the Moon. *J. Geophys. Res. Planets* **2014**, *119*, 976–997. [CrossRef]
49. Kramer, G.Y.; Besse, S.; Nettles, J.; Combe, J.P.; Clark, R.N.; Pieters, C.M.; Staid, M.; Malaret, E.; Boardman, J.; Green, R.O. Newer views of the Moon: Comparing spectra from Clementine and the Moon Mineralogy Mapper. *J. Geophys. Res. Planets* **2011**, *116*, e2010JE003728. [CrossRef]
50. Oliveira, J.S.; Vervelidou, F.; Wieczorek, M.A.; Michelena, M.D. Constraints on the Spatial Distribution of Lunar Crustal Magnetic Sources From Orbital Magnetic Field Data. *J. Geophys. Res. Planets* **2024**, *129*, e2023JE008125. [CrossRef]
51. Hood, L.; Zakharian, A.; Halekas, J.; Mitchell, D.; Lin, R.; Acuña, M.; Binder, A. Initial mapping and interpretation of lunar crustal magnetic anomalies using Lunar Prospector magnetometer data. *J. Geophys. Res. Planets* **2001**, *106*, 27825–27839. [CrossRef]
52. Nicholas, J.B.; Purucker, M.E.; Sabaka, T.J. Age spot or youthful marking: Origin of Reiner Gamma. *Geophys. Res. Lett.* **2007**, *34*, L02205. [CrossRef]
53. Bando, Y.; Kumamoto, A.; Nakamura, N. Constraint on subsurface structures beneath Reiner Gamma on the Moon using the Kaguya Lunar Radar Sounder. *Icarus* **2015**, *254*, 144–149. [CrossRef]
54. Wen, S.; Wang, Y.; Gong, Q.; Liu, J.; Kang, X.; Liu, H.; Chen, R.; Zhu, K.; Zhang, S. A New Robust Lunar Landing Selection Method Using the Bayesian Optimization of Extreme Gradient Boosting Model (BO-XGBoost). *Remote Sens.* **2024**, *16*, 3632. [CrossRef]
55. Lemelin, M.; Lucey, P.G.; Miljkovic, K.; Gaddis, L.R.; Hare, T.; Ohtake, M. The compositions of the lunar crust and upper mantle: Spectral analysis of the inner rings of lunar impact basins. *Planet. Space Sci.* **2019**, *165*, 230–243. [CrossRef]
56. Lemelin, M.; Lucey, P.G.; Song, E.; Taylor, G.J. Lunar central peak mineralogy and iron content using the Kaguya Multi-band Imager: Reassessment of the compositional structure of the lunar crust. *J. Geophys. Res. Planets* **2015**, *120*, 869–887. [CrossRef]
57. Taylor, L.A.; Pieters, C.; Patchen, A.; Taylor, D.H.S.; Morris, R.V.; Keller, L.P.; Mckay, D.S. Mineralogical and chemical characterization of lunar highland soils: Insights into the space weathering of soils on airless bodies. *J. Geophys. Res. Planets* **2010**, *115*, e2009je003427. [CrossRef]
58. Zhang, L.; Zhang, X.; Yang, M.; Xiao, X.; Qiu, D.; Yan, J.; Xiao, L.; Huang, J. New maps of major oxides and Mg # of the lunar surface from additional geochemical data of Chang'E-5 samples and KAGUYA multiband imager data. *Icarus* **2023**, *397*, 115505. [CrossRef]
59. Cavanaugh, J.F.; Smith, J.C.; Sun, X.L.; Bartels, A.E.; Ramos-Izquierdo, L.; Krebs, D.J.; McGarry, J.F.; Trunzo, R.; Novo-Gradac, A.M.; Britt, J.L.; et al. The Mercury Laser Altimeter instrument for the MESSENGER mission. *Space Sci. Rev.* **2007**, *131*, 451–479. [CrossRef]
60. Smith, D.E.; Zuber, M.T.; Frey, H.V.; Garvin, J.B.; Head, J.W.; Muhleman, D.O.; Pettengill, G.H.; Phillips, R.J.; Solomon, S.C.; Zwally, H.J.; et al. Mars Orbiter Laser Altimeter: Experiment summary after the first year of global mapping of Mars. *J. Geophys. Res. Planets* **2001**, *106*, 23689–23722. [CrossRef]
61. Smith, D.E.; Zuber, M.T.; Neumann, G.A.; Lemoine, F.G.; Mazarico, E.; Torrence, M.H.; McGarry, J.F.; Rowlands, D.D.; Head, J.W.; Duxbury, T.H.; et al. Initial observations from the Lunar Orbiter Laser Altimeter (LOLA). *Geophys. Res. Lett.* **2010**, *37*, e2010gl043751. [CrossRef]
62. Mazarico, E.; Rowlands, D.D.; Neumann, G.A.; Smith, D.E.; Torrence, M.H.; Lemoine, F.G.; Zuber, M.T. Orbit determination of the Lunar Reconnaissance Orbiter. *J. Geod.* **2012**, *86*, 193–207. [CrossRef]

63. Barker, M.K.; Mazarico, E.; Neumann, G.A.; Zuber, M.T.; Haruyama, J.; Smith, D.E. A new lunar digital elevation model from the Lunar Orbiter Laser Altimeter and SELENE Terrain Camera. *Icarus* **2016**, *273*, 346–355. [CrossRef]
64. Liu, Q.; Cheng, W.; Yan, G. Distribution characteristics and classification schemes of lunar surface elevation. *Acta Geogr. Sin.* **2021**, *76*, 106–119. [CrossRef]
65. Sun, Z.; Jia, Y.; Zhang, H. Technological advancements and promotion roles of Chang'e-3 lunar probe mission. *Sci. China Technol. Sci.* **2013**, *56*, 2702–2708. [CrossRef]
66. Deng, J. *Classification of Lunar Landforms Coupled with Morphology and Genesis and Intelligent Identification of Impact Landforms*; University of Chinese Academy of Sciences: Beijing, China, 2023.
67. Kreslavsky, M.A.; Head, J.W.; Neumann, G.A.; Rosenburg, M.A.; Aharonson, O.; Smith, D.E.; Zuber, M.T. Lunar topographic roughness maps from Lunar Orbiter Laser Altimeter (LOLA) data: Scale dependence and correlation with geologic features and units. *Icarus* **2013**, *226*, 52–66. [CrossRef]
68. Deng, J.Y.; Cheng, W.M.; Liu, Q.Y.; Jiao, Y.M.; Liu, J.Z. Morphological differentiation characteristics and classification criteria of lunar surface relief amplitude. *J. Geogr. Sci.* **2022**, *32*, 2365–2378. [CrossRef]
69. Bandfield, J.L.; Hayne, P.; Williams, J.P.; Greenhagen, B.T.; Paige, D.A. Lunar surface roughness derived from LRO Diviner Radiometer observations. *Icarus* **2015**, *248*, 357–372. [CrossRef]
70. Chen, J.; Ling, Z.C.; Liu, J.Z.; Chen, S.B.; Ding, X.Z.; Chen, J.P.; Cheng, W.M.; Li, B.; Zhang, J.; Sun, L.Z.; et al. Digital and global lithologic mapping of the Moon at a 1:2,500,000 scale. *Sci. Bull.* **2022**, *67*, 2050–2054. [CrossRef]
71. Guo, D.; Liu, J.; Head, J.W.; Zhang, F.; Ling, Z.; Chen, S.; Chen, J.; Ding, X.; Ji, J.; Ouyang, Z. A lunar time scale from the perspective of the Moon's dynamic evolution. *Sci. China Earth Sci.* **2023**, *67*, 234–251. [CrossRef]
72. Ji, J.Z.; Guo, D.J.; Liu, J.Z.; Chen, S.B.; Ling, Z.C.; Ding, X.Z.; Han, K.Y.; Chen, J.P.; Cheng, W.M.; Zhu, K.; et al. The 1:2,500,000-scale geologic map of the global Moon. *Sci. Bull.* **2022**, *67*, 1544–1548. [CrossRef]
73. Liu, J.; Liu, J.; Yue, Z.; Zhang, L.; Wang, J.; Zhu, K. Characterization and interpretation of the global lunar impact basins based on remote sensing. *Icarus* **2022**, *378*, 114952. [CrossRef]
74. Lu, T.Q.; Zhu, K.; Chen, S.B.; Liu, J.Z.; Ling, Z.C.; Ding, X.Z.; Han, K.Y.; Chen, J.P.; Cheng, W.M.; Lei, D.H.; et al. The 1:2,500,000-scale global tectonic map of the Moon. *Sci. Bull.* **2022**, *67*, 1962–1966. [CrossRef]
75. Housen, K.R. Crater Ejecta Scaling Laws. *J. Geophys. Res.* **1983**, *88*, 2485–2499. [CrossRef]
76. Hiesinger, H.; Head, J.W.; Wolf, U.; Jaumann, R.; Neukum, G. Ages and stratigraphy of mare basalts in Oceanus Procellarum, Mare Nubium, Mare Cognitum, and Mare Insularum. *J. Geophys. Res. Planets* **2003**, *108*, e2002je001985. [CrossRef]
77. Hiesinger, H.; Head, J.W.; Wolf, U.; Jaumann, R.; Neukum, G. Ages and stratigraphy of lunar mare basalts: A synthesis. In *Recent Advances and Current Research Issues in Lunar Stratigraphy (Geological Society of America Special Paper)*; Geological Society of America: Boulder, CO, USA, 2011; pp. 1–52.
78. Taylor, L.A.; Pieters, C.M.; Keller, L.P.; Morris, R.V.; McKay, D.S. Lunar Mare Soils: Space weathering and the major effects of surface-correlated nanophase Fe. *J. Geophys. Res. Planets* **2001**, *106*, 27985–27999. [CrossRef]
79. Deca, J.; Hemingway, D.J.; Divin, A.; Lue, C.; Poppe, A.R.; Garrick-Bethell, I.; Lembège, B.; Horányi, M. Simulating the Reiner Gamma Swirl: The Long-Term Effect of Solar Wind Standoff. *J. Geophys. Res. Planets* **2020**, *125*, e2019JE006219. [CrossRef]
80. Deca, J.; Poppe, A.R.; Divin, A.; Lembège, B. The Plasma Environment Surrounding the Reiner Gamma Magnetic Anomaly. *J. Geophys. Res. Space Phys.* **2021**, *126*, e2021JA029180. [CrossRef]
81. Jiang, Z.; Ling, Z.; Bo, L.; Wu, Z. Photometric behaviors and classification of Reiner Gamma swirl materials. *Acta Petrol. Sin.* **2016**, *32*, 113–118.
82. Poppe, A.R.; Fatemi, S.; Garrick-Bethell, I.; Hemingway, D.; Holmström, M. Solar wind interaction with the Reiner Gamma crustal magnetic anomaly: Connecting source magnetization to surface weathering. *Icarus* **2016**, *266*, 261–266. [CrossRef]
83. Walker, R.T.; Barker, M.K.; Mazarico, E.; Sun, X.; Neumann, G.A.; Smith, D.E.; Head, J.W.; Zuber, M.T. Near-infrared Pho-tometry of the Moon's Surface with Passive Radiometry from the Lunar Orbiter Laser Altimeter (LOLA). *Planet. Sci. J.* **2024**, *5*, 122. [CrossRef]
84. Carporzen, L.; Weiss, B.P.; Elkins-Tanton, L.T.; Shuster, D.L.; Ebel, D.; Gattacceca, J. Magnetic evidence for a partially differentiated carbonaceous chondrite parent body. *Proc. Natl. Acad. Sci. USA* **2011**, *108*, 6386–6389. [CrossRef]
85. Cournede, C.; Gattacceca, J.; Gounelle, M.; Rochette, P.; Weiss, B.P.; Zanda, B. An early solar system magnetic field recorded in CM chondrites. *Earth Planet. Sci. Lett.* **2015**, *410*, 62–74. [CrossRef]
86. Fu, R.R.; Lima, E.A.; Weiss, B.P. No nebular magnetization in the Allende CV carbonaceous chondrite. *Earth Planet. Sci. Lett.* **2014**, *404*, 54–66. [CrossRef]
87. Weiss, B.P.; Berdahl, J.S.; Elkins-Tanton, L.; Stanley, S.; Lima, E.A.; Carporzen, L. Magnetism on the Angrite Parent Body and the Early Differentiation of Planetesimals. *Science* **2008**, *322*, 713–716. [CrossRef] [PubMed]
88. Zhang, Y.C.; Stevens, J.G.; Li, Y.S.; Li, Z.L. Mossbauer Study of the Jilin and Xinyang Meteorites. *Hyperfine Interact* **1994**, *91*, 547–550. [CrossRef]
89. Borg, L.E.; Cassata, W.S.; Wimpenny, J.; Gaffney, A.M.; Shearer, C.K. The formation and evolution of the Moon's crust inferred from the Sm-Nd isotopic systematics of highlands rocks. *Geochim. Et Cosmochim. Acta* **2020**, *290*, 312–332. [CrossRef]
90. Charlier, B.; Grove, T.L.; Namur, O.; Holtz, F. Crystallization of the lunar magma ocean and the primordial mantle-crust differentiation of the Moon. *Geochim. Cosmochim. Acta* **2018**, *234*, 50–69. [CrossRef]

91. Johnson, T.E.; Morrissey, L.J.; Nemchin, A.A.; Gardiner, N.J.; Snape, J.F. The phases of the Moon: Modelling crystallisation of the lunar magma ocean through equilibrium thermodynamics. *Earth Planet. Sci. Lett.* **2021**, *556*, 116721. [CrossRef]
92. Rapp, J.F.; Draper, D.S. Fractional crystallization of the lunar magma ocean: Updating the dominant paradigm. *Meteorit. Planet. Sci.* **2018**, *53*, 1432–1455. [CrossRef]
93. Snyder, G.A.; Taylor, L.A.; Neal, C.R. A Chemical-Model for Generating the Sources of Mare Basalts—Combined Equilibrium and Fractional Crystallization of the Lunar Magmasphere. *Geochim. et Cosmochim. Acta* **1992**, *56*, 3809–3823. [CrossRef]
94. Wieczorek, M.A.; Neumann, G.A.; Nimmo, F.; Kiefer, W.S.; Taylor, G.J.; Melosh, H.J.; Phillips, R.J.; Solomon, S.C.; Andrews-Hanna, J.C.; Asmar, S.W.; et al. The Crust of the Moon as Seen by GRAIL. *Science* **2013**, *339*, 671–675. [CrossRef] [PubMed]
95. Borg, L.E.; Shearer, C.K.; Asmerom, Y.; Papike, J.J. Prolonged KREEP magmatism on the Moon indicated by the youngest dated lunar igneous rock. *Nature* **2004**, *432*, 209–211. [CrossRef]
96. Elardo, S.M.; Laneuville, M.; McCubbin, F.M.; Shearer, C.K. Early crust building enhanced on the Moon's nearside by mantle melting-point depression. *Nat. Geosci.* **2020**, *13*, 339–343. [CrossRef]
97. Lin, Y.H.; Tronche, E.J.; Steenstra, E.S.; van Westrenen, W. Experimental constraints on the solidification of a nominally dry lunar magma ocean. *Earth Planet. Sci. Lett.* **2017**, *471*, 104–116. [CrossRef]
98. Shearer, C.K.; Elardo, S.M.; Petro, N.E.; Borg, L.E.; McCubbin, F.M. Origin of the lunar highlands Mg-suite: An integrated petrology, geochemistry, chronology, and remote sensing perspective. *Am. Mineral.* **2015**, *100*, 294–325. [CrossRef]
99. Whitten, J.; Head, J.W.; Staid, M.; Pieters, C.M.; Mustard, J.; Clark, R.; Nettles, J.; Klima, R.L.; Taylor, L. Lunar mare deposits associated with the Orientale impact basin: New insights into mineralogy, history, mode of emplacement, and relation to Orientale Basin evolution from Moon Mineralogy Mapper (M3) data from Chandrayaan-1. *J. Geophys. Res.* **2011**, *116*, e2010je003736. [CrossRef]
100. Whitten, J.L.; Head, J.W. Lunar cryptomaria: Physical characteristics, distribution, and implications for ancient volcanism. *Icarus* **2015**, *247*, 150–171. [CrossRef]
101. Shea, E.K.; Weiss, B.P.; Cassata, W.S.; Shuster, D.L.; Tikoo, S.M.; Gattacceca, J.; Grove, T.L.; Fuller, M.D. A Long-Lived Lunar Core Dynamo. *Science* **2012**, *335*, 453–456. [CrossRef]
102. Suavet, C.; Weiss, B.P.; Cassata, W.S.; Shuster, D.L.; Gattacceca, J.; Chan, L.; Garrick-Bethell, I.; Head, J.W.; Grove, T.L.; Fuller, M.D. Persistence and origin of the lunar core dynamo. *Proc. Natl. Acad. Sci. USA* **2013**, *110*, 8453–8458. [CrossRef]
103. Tikoo, S.M.; Weiss, B.P.; Buz, J.; Lima, E.A.; Shea, E.K.; Melo, G.; Grove, T.L. Magnetic fidelity of lunar samples and implications for an ancient core dynamo. *Earth Planet. Sci. Lett.* **2012**, *337*, 93–103. [CrossRef]
104. Hiesinger, M.H.; Gebhart, J.; van der Bogert, C.; Pasckert, J.; Weinauer, J.; Lawrence, S.; Stopar, J.; Robinson, M. Stratigraphy of low shields and mare basalts of the Marius Hills region. In Proceedings of the Lunar and Planetary Science Conference, Woodland, TX, USA, 21–25 March 2016.
105. Lawrence, S.J.; Stopar, J.D.; Hawke, B.R.; Greenhagen, B.T.; Cahill, J.T.; Bandfield, J.L.; Jolliff, B.L.; Denevi, B.W.; Robinson, M.S.; Glotch, T.D. LRO observations of morphology and surface roughness of volcanic cones and lobate lava flows in the Marius Hills. *J. Geophys. Res. Planets* **2013**, *118*, 615–634. [CrossRef]
106. Tikoo, S.M.; Weiss, B.P.; Cassata, W.S.; Shuster, D.L.; Gattacceca, J.; Lima, E.A.; Suavet, C.; Nimmo, F.; Fuller, M.D. Decline of the lunar core dynamo. *Earth Planet. Sci. Lett.* **2014**, *404*, 89–97. [CrossRef]

Disclaimer/Publisher's Note: The statements, opinions and data contained in all publications are solely those of the individual author(s) and contributor(s) and not of MDPI and/or the editor(s). MDPI and/or the editor(s) disclaim responsibility for any injury to people or property resulting from any ideas, methods, instructions or products referred to in the content.